

# Fast Continuum Robot Shape and External Load State Estimation on SE(3)

James M. Ferguson<sup>1</sup>, Alan Kuntz<sup>1</sup>, and Tucker Hermans<sup>1,2</sup>

**Abstract**— Previous on-manifold approaches to continuum robot state estimation have typically adopted simplified Cosserat rod models, which cannot directly account for actuation inputs or external loads. We introduce a general framework that incorporates uncertainty models for actuation (e.g., tendon tensions), applied forces and moments, process noise, boundary conditions, and arbitrary backbone measurements. By adding temporal priors across time steps, our method additionally performs joint estimation in both the spatial (arclength) and temporal domains, enabling full *spacetime* state estimation. Discretizing the arclength domain yields a factor graph representation of the continuum robot model, which can be exploited for fast batch sparse nonlinear optimization in the style of SLAM. The framework is general and applies to a broad class of continuum robots; as illustrative cases, we show (i) tendon-driven robots in simulation, where we demonstrate real-time kinematics with uncertainty, tip force sensing from position feedback, and distributed load estimation from backbone strain, and (ii) a surgical concentric tube robot in experiment, where we validate accurate kinematics and tip force estimation, highlighting potential for surgical palpation.

## I. INTRODUCTION

Continuum robots are thin, tentacle-like manipulators whose backbones deform continuously in response to actuation or external loading. Their slender shape and inherent compliance make them particularly well-suited for medical applications [1]. The primary objective of modeling continuum robots is to predict the backbone shape in response to actuation (e.g., tendon tensions), specifically the pose  $T(s) \in \text{SE}(3)$  at any arclength position. This is classically approached deterministically, by solving a boundary value problem in arclength where the Cosserat rod equations act as a hard dynamic constraint [2].

An important secondary objective is to quantify the uncertainty of backbone predictions, since even accurate robot models are affected by unmodeled effects and actuation uncertainty. Furthermore, uncertainty can be tamed by external observations, which motivates state estimation approaches. While many approaches parameterize pose with vectors [3]–[5], it is increasingly common to operate directly on  $\text{SE}(3)$ , storing poses as homogeneous transformations and applying perturbations in the tangent space. Such on-manifold estimation has been widely adopted in mobile robotics for localization, mapping, and navigation [6]–[9],

\*Research reported in this publication was supported by the Advanced Research Projects Agency for Health (ARPA-H) under Award Number D24AC00415-00. The ARPA-H award provided 100% of total costs with an award total of up to \$11,935,038. The content is solely the responsibility of the authors and does not necessarily represent the official views of ARPA-H.)

<sup>1</sup>Authors are with the Kahlert School of Computing and Robotics Center, University of Utah, USA. <sup>2</sup>NVIDIA, Seattle, WA, USA. Correspondence: j.m.ferguson@utah.edu

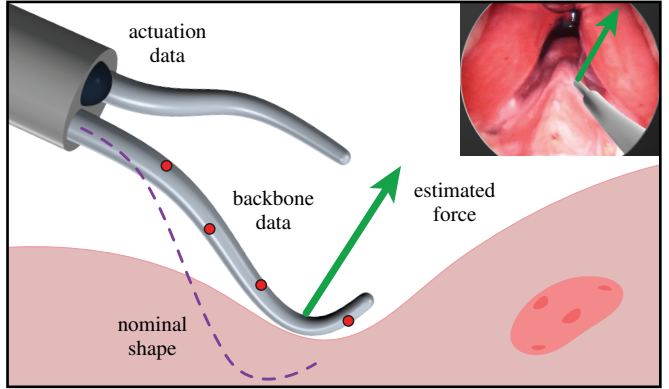


**Fig. 1:** Conceptual illustration of our approach applied to a surgical robot. Our method fuses uncertain actuation inputs and external backbone measurements with a prior mechanics model to estimate shape and external loads. Our factor-graph formulation enables principled, real-time estimation of all states and uncertainties.

and is now emerging in continuum robotics, where similar time-domain estimation techniques are repurposed for the arclength domain [10], [11]. Prior on-manifold approaches to continuum robot state estimation use simplified motion priors, effectively modeling strain dynamics as noise, and cannot incorporate actuation or external load variables.

In this work, we leverage efficient, sparse nonlinear optimization (e.g., GTSAM [12]), to solve the full Cosserat rod equations on  $\text{SE}(3)$ , enabling posterior distributions over backbone pose, internal stresses, actuation inputs, and external loads from arbitrary measurements. Our formulation is built on a discrete-arclength factor graph representation of the Cosserat rod, which preserves accuracy through a midpoint discretization strategy. The resulting framework is general and applicable to a wide range of continuum robots. We demonstrate its accuracy and versatility in tendon-driven robot simulations (shape, tip wrench, and distributed load estimation) and validate it experimentally on a surgical concentric tube robot, achieving real-time pose and tip-force estimation with potential application to surgical palpation.

## II. RELATED WORK

While early approaches to continuum robot shape estimation focused on geometric curve fitting [13]–[15], recent approaches use fiber Bragg grating sensors [16], [17], which directly integrate pose from strain measurements, but can suffer from dead-reckoning effects if uncertainty is not accounted for. Recent learning-based approaches have also been explored, using neural networks to regress backbone shape from observed data [18]. Such methods can achieve

high accuracy within a trained regime, but typically require retraining or adaptation for each new robot or sensing setup.

In parallel, several groups pursued physics-based optimization methods that fit Cosserat rod models to data. For example, Black et al. estimate tip forces in tendon-driven robots via optimization [19], while Aloi et al. optimize distributed external loads to reduce measured shape residuals [20]. These deterministic fitting approaches lack principled treatment of uncertainty, a critical need when solving ill-conditioned problems inherent to continuum robots [5], [20].

This motivates probabilistic formulations of Cosserat models. Rucker et al. introduced deflection-based force sensing, using backbone deflections to infer a distribution over applied tip forces [21]. Several Kalman-based methods have been successful for continuum robot guidance and force sensing in surgery [22]–[24]. Mahoney et al. and Anderson et al. were the first to solve the Cosserat equations as a stochastic process in arclength, combining process and measurement noise within filtering frameworks [3], [4]. More recently, Ferguson et al. presented a unified Bayesian framework for shape and external load estimation [5]. All of these methods, however, adopt vector-space state representations of  $SE(3)$  which introduce representational singularities.

Thus, on-manifold methods have recently gained attention. Most relevant to our work is Lilge et al. [10], [11], who applied Gaussian process regression on  $SE(3)$  with a continuous Cosserat prior. While elegant and efficient for geometric estimation, their prior is limited to passive backbone mechanics and cannot incorporate actuation inputs or distributed external loads (e.g. for force sensing).

Collocation methods [25], [26] and other weighted residual formulations [27], [28] have been applied to continuum robots and are conceptually related to our approach, since they discretize arclength into nodes, and enforce the Cosserat equations either pointwise (collocation) or in an averaged sense (Galerkin, Ritz). While effective, these approaches are not designed for state estimation or to quantify uncertainty.

In contrast, factor-graph based sparse nonlinear optimization has proven remarkably effective for estimation problems in robotics, including Simultaneous Localization and Mapping (SLAM) [9], forward and inverse dynamics [29], constrained trajectory optimization [30], [31], and motion planning [32]. While these methods estimate *temporal* trajectories of rigid or articulated robots, we instead estimate *spatial* trajectories of flexible continuum robots.

### III. COSSERAT ROD MODEL

To model continuum robot backbones, we adopt the Cosserat rod formulation of Pai et al. [33], later formalized for state estimation by Lilge et al. [10]. We use the convention that pose  $\mathbf{T}(s) \in SE(3)$  maps body coordinates to spatial coordinates, and Lie algebra elements such as the generalized strain  $\boldsymbol{\varepsilon}(s) \in \mathfrak{se}(3)$  are represented with their rotational components first. The Cosserat kinematic equation prescribe that pose evolves in arclength according to

$$\frac{d}{ds} \mathbf{T}(s) = \mathbf{T}(s) \boldsymbol{\varepsilon}(s)^\wedge, \quad \boldsymbol{\varepsilon}(s) = \begin{bmatrix} \boldsymbol{\omega}(s) \\ \boldsymbol{\nu}(s) \end{bmatrix} \quad (1)$$

where  $\boldsymbol{\omega}(s)$  and  $\boldsymbol{\nu}(s)$  are the angular rate and linear rates respectively and  $\boldsymbol{\varepsilon}(s)^\wedge = [\boldsymbol{\omega}(s)^\wedge \quad \boldsymbol{\nu}(s); \ 0 \ 0]$ , where  $(\cdot)^\wedge$  is the standard hat operator mapping  $\mathbb{R}^3$  to skew matrices (i.e.  $\boldsymbol{\omega}^\wedge \boldsymbol{v} = \boldsymbol{\omega} \times \boldsymbol{v}$ ).

The generalized strain  $\boldsymbol{\varepsilon}(s) \in \mathbb{R}^6$  is analogous to generalized velocity (body frame) in rigid body motion and deviates from its nominal, stress-free value  $\bar{\boldsymbol{\varepsilon}}(s)$  under loading based on the material constitutive law

$$\boldsymbol{\sigma}(s) = \begin{bmatrix} \mathbf{m}(s) \\ \mathbf{n}(s) \end{bmatrix} = \mathcal{K}(\boldsymbol{\varepsilon}(s) - \bar{\boldsymbol{\varepsilon}}(s)) \quad (2)$$

which relates the generalized stress  $\boldsymbol{\sigma}(s)$ —comprising internal moment  $\mathbf{m}(s)$  and force  $\mathbf{n}(s)$ —to the strain through the stiffness matrix  $\mathcal{K}$ , which encodes sensitivity to shear, elongation, bending, and torsion.

Lilge et al. [10] highlighted the similarity of the Cosserat rod model [33] to classical rigid body dynamics, with the following differential relationship between stress, strain, and the external distributed wrench  $\mathbf{f}(s) \in \mathbb{R}^6$  along the rod. Rewriting in our frame convention:

$$\frac{d}{ds} \boldsymbol{\sigma}(s) = \text{ad}_{\boldsymbol{\varepsilon}(s)}^T \boldsymbol{\sigma}(s) - \mathbf{f}(s), \quad (3)$$

where  $\text{ad}_{\boldsymbol{\varepsilon}(s)} = [\boldsymbol{\omega}(s)^\wedge \quad 0; \ \boldsymbol{\nu}(s)^\wedge \quad \boldsymbol{\omega}(s)^\wedge]$ . The trouble is that the stresses and strains (caused by e.g. tendon actuation) are nonlinearly coupled to the shape of the robot. In fact, all previous approaches for continuum robot estimation on  $SE(3)$  have made a fairly extreme approximation, lumping all of the unknowns into a single white noise process, resulting in the following simplified motion prior:

$$\frac{d}{ds} \mathbf{T}(s) = \mathbf{T}(s) \boldsymbol{\varepsilon}(s)^\wedge, \quad \frac{d}{ds} \boldsymbol{\varepsilon}(s) \sim \text{white noise}. \quad (4)$$

While this model works remarkably well when external sensing is available, (4) cannot incorporate actuation variables (e.g. tendon tensions) or reason over external loads (e.g. from environmental contact).

While previous approaches focus on continuous arclength representations [5], [10], [11], we instead discretize the arclength domain and show that in discrete arclength, it is straightforward to explicitly take actuation and external loading into account, and we can readily exploit existing sparse solvers (e.g. GTSAM [12]) enabling real time solutions. Furthermore, when using a midpoint rule, we demonstrate good numerical accuracy compared to a numerical integration benchmark. The discretization approach is similar to [34], but our solution is based on sparse nonlinear optimization using factor graphs.

Swapping time for arclength, the discrete version of the Cosserat kinematics is exactly the same as rigid body kinematics (e.g. in [6]). Assuming that strain  $\boldsymbol{\varepsilon}_k = \boldsymbol{\varepsilon}(s_k)$  is constant over the interval  $[s_k, s_{k+1}]$  and  $\Delta s = s_{k+1} - s_k$  is spatially uniform, the discrete version of (1) is

$$\mathbf{T}_{k+1} = \mathbf{T}_k \exp(\Delta s \boldsymbol{\varepsilon}_k^\wedge). \quad (5)$$

Note that we write all unknown variables to be estimated in bold, roman, uppercase type (e.g.  $\mathbf{T}_k = \mathbf{T}(s_k)$ ).

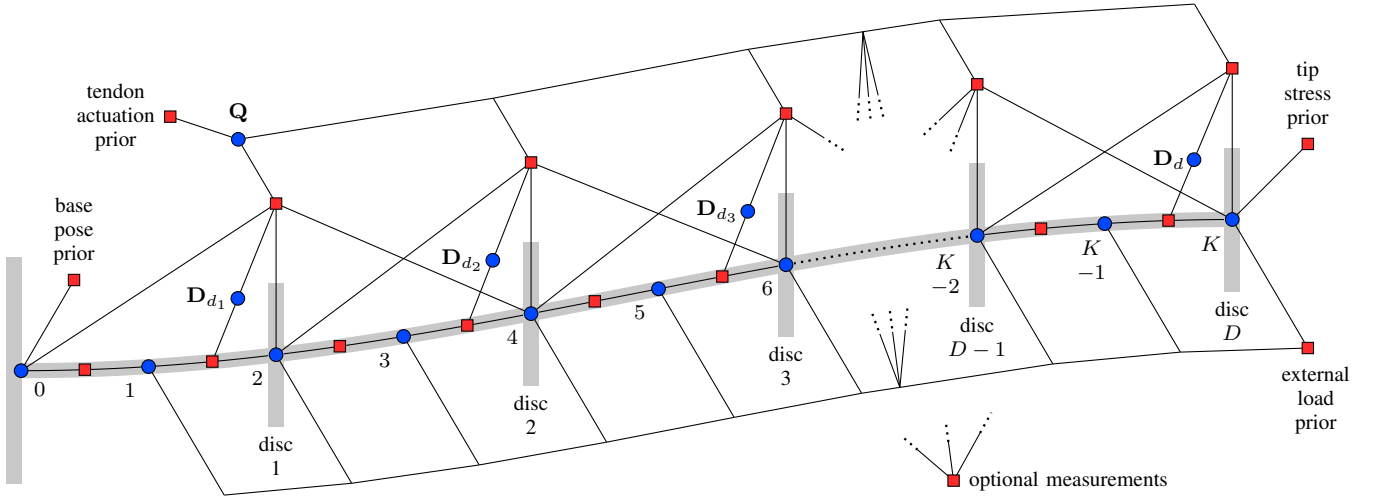


**Fig. 2:** Factor graph representation of the discrete Cosserat rod model with tendon actuation, assuming only one node between each disc for clarity. Each of the  $K$  nodes along the rod includes pose  $\mathbf{T}_k$ , internal stress  $\mathbf{S}_k$ , and external wrench  $\mathbf{F}_k$ . Given actuation tensions  $\mathbf{Q}$ , the graph models forward kinematics with uncertainty. The inverse problem—estimating  $\mathbf{F}_k$ —is solved by attaching measurement factors to backbone states (e.g.,  $\mathbf{T}_k$ ,  $\mathbf{S}_k$ ). External load  $\mathbf{F}_k$  priors are chosen based on sensing application (e.g., tip forces only), and we also include temporal priors to smooth over time, as well as spatial priors along the rod for distributed loads.

Now by rearranging (2) and adding Gaussian noise, the generalized strain  $\varepsilon_k$  is related to stress  $\mathbf{S}_k = \boldsymbol{\sigma}(s_k)$  by:

$$\varepsilon_k = \mathcal{K}^{-1} \mathbf{S}_k + \bar{\varepsilon}_k + \mathbf{n}_{T_k}, \quad \mathbf{n}_{T_k} \sim \mathcal{N}(0, \Sigma_T), \quad (6)$$

where  $\bar{\varepsilon}_k$  encodes the nominal shape of the rod in its unstressed state. Thus,  $\mathbf{n}_{T_k}$  models uncertainty in the initial shape of the rod, as well as any deviations from the linear constitutive law. The above formulation is akin to an Euler integration method, where  $\varepsilon_k$  is used to propagate  $\mathbf{T}_k$  to  $\mathbf{T}_{k+1}$ , but we found that significant pose accuracy gains can be had by instead using a midpoint rule:

$$\varepsilon_k = \frac{1}{2} \mathcal{K}^{-1} (\mathbf{S}_k + \mathbf{S}_{k+1}) + \bar{\varepsilon} + \mathbf{n}_{\varepsilon_k}, \quad (7)$$

where generalized strain is computed based on the average of the two stresses  $\mathbf{S}_k$  and  $\mathbf{S}_{k+1}$ .

To discretize the Cosserat mechanics (3), we rewrite in the spatial ( $w$ ) frame and assume that all of the distributed load is concentrated at the  $K$  node locations:

$$\frac{d}{ds} \boldsymbol{\sigma}^w(s) = -\mathbf{f}^w(s) = -\sum_{k=1}^K \delta(s - s_k) \mathbf{f}_k^w. \quad (8)$$

Since  $\frac{d}{ds} \boldsymbol{\sigma}^w(s) = 0$  on the interior of the segment, we can evaluate directly on the endpoints and add the point wrench at  $k+1$ :

$$\boldsymbol{\sigma}^w(s_{k+1}) = \boldsymbol{\sigma}^w(s_k) - \mathbf{f}_{k+1}^w \quad (9)$$

Rewriting back in the body frame, manipulating, and allowing for Gaussian noise, we arrive at

$$\mathbf{S}_{k+1} = \mathbf{A}^T (\mathbf{T}_k^{-1} \mathbf{T}_{k+1}) \mathbf{S}_k - \mathbf{f}_{k+1} + \mathbf{n}_{S_k}. \quad (10)$$

In practice, we set the noise level  $\mathbf{n}_{S_k} \sim \mathcal{N}(0, \Sigma_S)$  in this equation to a small value to softly enforce equality. We note that (10) is not a difference equation but instead an exact integration (assuming concentrated wrenches), which

we combine with our kinematics equations (7), (5) for our full Cosserat model.

To anchor the chain of poses (5) and the chain of internal stresses (10), we place priors on both the robot base frame and the internal stress at the tip:

$$\begin{aligned} \mathbf{T}_0 &= \bar{\mathbf{T}}_0 \exp(\xi_0^\wedge) & \xi_0 &\sim \mathcal{N}(\mathbf{0}, \Sigma_0) \\ \mathbf{S}_K &= \mathbf{0} + \mathbf{n}_K & \mathbf{n}_K &\sim \mathcal{N}(\mathbf{0}, \Sigma_K). \end{aligned} \quad (11)$$

Encoding constraints as priors is common in state estimation and additionally allows for incorporation of uncertainty (e.g. the base pose is not perfectly known).

Thus, given prior knowledge of  $\mathbf{f}_k$ , we could solve for the Maximum a Posteriori (MAP) states  $\mathbf{T}_k$  and  $\mathbf{S}_k$  using (5), (7), (10), and (11) as residuals. However, loads are typically not known a priori, and in the case of tendon actuation, they are coupled to rod shape  $\mathbf{T}_k$ .

#### IV. TENDON ACTUATION

Here we develop a probabilistic model linking tendon tensions actuation  $\mathbf{Q} \in \mathbb{R}^N$  to the loads  $\mathbf{f}_k$  distributed along the discrete Cosserat rod robot backbone. The overall relationship is based on [35], but we include uncertainty in order to build a factor graph representation of the full robot.

We assume that the tendon routing discs are coincident with a subset of the arclength nodes:  $\mathcal{D} = \{d_0, d_1, \dots, D\} \subseteq \{0, 1, \dots, K\}$ . For nodes which do not have discs ( $k \notin \mathcal{D}$ ), we simply use the unknown external load wrench  $\mathbf{f}_k = \mathbf{F}_k$ . For nodes at discs ( $k \in \mathcal{D}$ ), we set  $\mathbf{f}_k = \mathbf{D}_d$  where

$$\mathbf{D}_d = \sum_{i=1}^N \left( \mathbf{f}_{d,i}^{d-1} + \mathbf{f}_{d,i}^{d+1} \right) + \mathbf{F}_d + \mathbf{n}_{D_d} \quad (12)$$

where the noise  $\mathbf{n}_{D_d} \sim \mathcal{N}(0, \Sigma_D)$  models small deviations such as tendon-disc friction. The wrenches  $\mathbf{f}_{d,i}^{d-1}$  and  $\mathbf{f}_{d,i}^{d+1}$  are due to the tensile force from tendon  $i$  in the direction

$$J(\mathbf{T}_{0:K}, \mathbf{S}_{0:K}, \mathbf{F}_{1:K}, \mathbf{D}_{1:D}, \mathbf{Q}) = J_0 + J_K + J_Q + \sum_{k=0}^{K-1} (J_{T_k} + J_{S_k}) + \sum_{k=1}^K J_{F_k} + \sum_{d=1}^D J_{D_d} + \sum_{m=1}^M J_{z_m} \quad (16)$$

where

$$\begin{aligned} J_0 &= \frac{1}{2} \mathbf{e}_0^T \Sigma_0^{-1} \mathbf{e}_0, & \mathbf{e}_0 &= \log \left( \bar{\mathbf{T}}_0^{-1} \mathbf{T}_0 \right)^\vee, & J_K &= \frac{1}{2} \mathbf{e}_K^T \Sigma_K^{-1} \mathbf{e}_K, & \mathbf{e}_K &= \mathbf{S}_K, & J_Q &= \frac{1}{2} \mathbf{e}_Q^T \Sigma_Q^{-1} \mathbf{e}_Q, & \mathbf{e}_Q &= \mathbf{Q} - \bar{\mathbf{Q}} \\ J_{F_k} &= \frac{1}{2} \mathbf{e}_{F_k}^T \Sigma_{F_k}^{-1} \mathbf{e}_{F_k}, & \mathbf{e}_{F_k} &= \mathbf{F}_k - \bar{\mathbf{F}}_k, & J_{D_d} &= \mathbf{e}_{D_d}^T \Sigma_D^{-1} \mathbf{e}_{D_d}, & \mathbf{e}_{D_d} &= \sum_{i=1}^N \left( \mathbf{f}_{d,i}^{d-1} + \mathbf{f}_{d,i}^{d+1} \right) + \mathbf{F}_d - \mathbf{D}_d \\ J_{T_k} &= \mathbf{e}_{T_k}^T \Sigma_T^{-1} \mathbf{e}_{T_k}, & \mathbf{e}_{T_k} &= \Delta s \left( \frac{1}{2} \mathcal{K}^{-1} (\mathbf{S}_k + \mathbf{S}_{k+1}) + \bar{\epsilon} \right) - \log \left( \mathbf{T}_k^{-1} \mathbf{T}_{k+1} \right)^\vee \\ J_{S_k} &= \mathbf{e}_{S_k}^T \Sigma_S^{-1} \mathbf{e}_{S_k}, & \mathbf{e}_{S_k} &= \mathbf{S}_{k+1} - \text{Ad}^T (\mathbf{T}_k^{-1} \mathbf{T}_{k+1}) \mathbf{S}_{k+1} + \mathbf{F}_{k+1} \end{aligned}$$

of the previous and next discs, and  $\mathbf{F}_{k=d}$  is any externally applied wrench at the disc.

The single tendon wrenches  $\mathbf{f}_{d,i}^j$ , due to the previous or next disc ( $j = \{d-1, d+1\}$ ) are computed based on the  $i^{\text{th}}$  tension  $q_i$  and the relative routing disc hole locations:

$$\begin{aligned} \mathbf{f}_{d,i}^j &= \begin{bmatrix} \mathbf{h}_{d,i}^\wedge \tilde{\mathbf{f}}_{d,i}^j \\ \tilde{\mathbf{f}}_{d,i}^j \end{bmatrix}, & \tilde{\mathbf{f}}_{d,i}^j &= q_i \frac{\mathbf{d}_{d,i}^j}{\|\mathbf{d}_{d,i}^j\|}, \\ \mathbf{d}_{d,i}^j &= [I_{3 \times 3} \ 0] \mathbf{T}_d^{-1} \mathbf{T}_j \begin{bmatrix} \mathbf{h}_{j,i} \\ 1 \end{bmatrix} - \mathbf{h}_{d,i}. \end{aligned} \quad (13)$$

Here the normalized difference in (body frame) hole locations  $\mathbf{h}_{d,i}$ ,  $\mathbf{h}_{j,i}$  is taken as the direction of the tendon force, scaled by  $q_i$ . Looking at (13), we see each  $\mathbf{D}_d$  is dependent on three disc poses  $\mathbf{T}_d$ ,  $\mathbf{T}_{d-1}$ ,  $\mathbf{T}_{d+1}$ , tensions  $\mathbf{Q}$ , and the external load  $\mathbf{F}_d$ .

Finally, we place prior factors on both the actuation variables and all external wrenches along the robot:

$$\begin{aligned} \mathbf{Q} &= \bar{\mathbf{Q}} + \mathbf{n}_Q & \mathbf{n}_Q &\sim \mathcal{N}(\mathbf{0}, \Sigma_Q) \\ \mathbf{F}_k &= \bar{\mathbf{F}}_k + \mathbf{n}_{F_k} & \mathbf{n}_{F_k} &\sim \mathcal{N}(\mathbf{0}, \Sigma_{F_k}). \end{aligned} \quad (14)$$

Typically,  $\bar{\mathbf{Q}}$  represents the measured tendon tensions, with sensor noise characterized by  $\Sigma_Q$ . The prior external wrench is usually unknown, so its mean  $\bar{\mathbf{F}}_k$  is set to zero, except during ground truth simulation. The wrench covariance  $\Sigma_{F_k}$  encodes prior belief: small when you assume no external load at  $k$  and large when you want to infer the force.

## V. ESTIMATION APPROACH

In the previous sections, we derived individual noise models for the Cosserat rod equations with tendon actuation. Here we combine these (along with noisy observations) into a posterior distribution and show the equivalent factor graph used for sparse MAP estimation.

Along with the measured tendon tensions  $\bar{\mathbf{Q}}$ , we may have access to several observations  $\mathbf{z}_k$  along the backbone of the robot (e.g. pose, strain, proximity). We define the measurement model

$$\mathbf{e}_{z_k} = \mathbf{g}(\mathbf{T}_k, \mathbf{S}_k, \mathbf{z}_k) + \mathbf{n}_z, \quad \mathbf{n}_z \sim \mathcal{N}(\mathbf{0}, \Sigma_{z_k}), \quad (15)$$

where  $\mathbf{g}$  computes the (possibly on-manifold) error between the observed  $\mathbf{z}_k$  and the state at node  $k$ . The cost of each measurement, compared to the model is  $J_{z_k} = \frac{1}{2} \mathbf{e}_{z_k}^T \Sigma_{z_k}^{-1} \mathbf{e}_{z_k}$ .

Given all of our Gaussian noise models, the full conditional negative log probability is proportional to a quadratic likelihood given by (16). Figure 2 illustrates the factor graph corresponding to the posterior distribution over robot state, actuation, and external loads.

### A. Sparse MAP Estimation

We implement a factor graph similar to Fig. 2 in GTSAM, where we evaluate Jacobians using GTSAM's built-in Lie group Jacobians, and then chain/product rule them all together as needed. Given tensions  $\mathbf{Q}$  and measurements  $\mathbf{z}_{0:K}$ , we use the dogleg optimizer to solve for the MAP estimate and take the Laplace approximation as the posterior. Since we solve a full optimization at each time step, we additionally warm start each optimization using the previous solution.

GTSAM enables efficient evaluation of marginal/joint covariances between arbitrary sets of variables [12]. In the specific case of pose variables, marginal distributions are represented as mean  $\bar{\mathbf{T}}_k \in SE(3)$  perturbed by the random twist  $\xi_k$ :

$$\mathbf{T}_k = \bar{\mathbf{T}}_k \exp(\hat{\xi}_k), \quad \xi_k \sim \mathcal{N}(0, \Sigma_{T_k T_k}). \quad (17)$$

### B. Resolved Rates Jacobian

Given the estimated state, we would additionally like to servo the robot to a desired configuration for closed loop control. This is typically accomplished using the Jacobian  $J_{T_K Q}$  relating actuation and local tool tip motion, which we can get from the Gaussian posterior. Indeed, we immediately have access to the joint covariance  $\Sigma_{T_K Q}$  between  $\mathbf{T}_K$  and  $\mathbf{Q}$ , as well as the marginal covariance  $\Sigma_{Q Q}$  so that the best linear predictor of  $\xi_k$  given  $\mathbf{Q}$  is

$$\begin{aligned} \mathbb{E}(\xi_K | \mathbf{Q}) &\approx \Sigma_{T_K Q} \Sigma_{Q Q}^{-1} (\mathbf{Q} - \bar{\mathbf{Q}}) = J_{T_K Q} \delta \mathbf{Q}, \\ \implies J_{T_K Q} &= \Sigma_{T_K Q} \Sigma_{Q Q}^{-1}, \end{aligned} \quad (18)$$

where we note that by definition of  $\xi_K$ , the Jacobian is in body frame coordinates. We use  $J_{T_K Q}$  for trajectory generation and feedback control in our experiments.

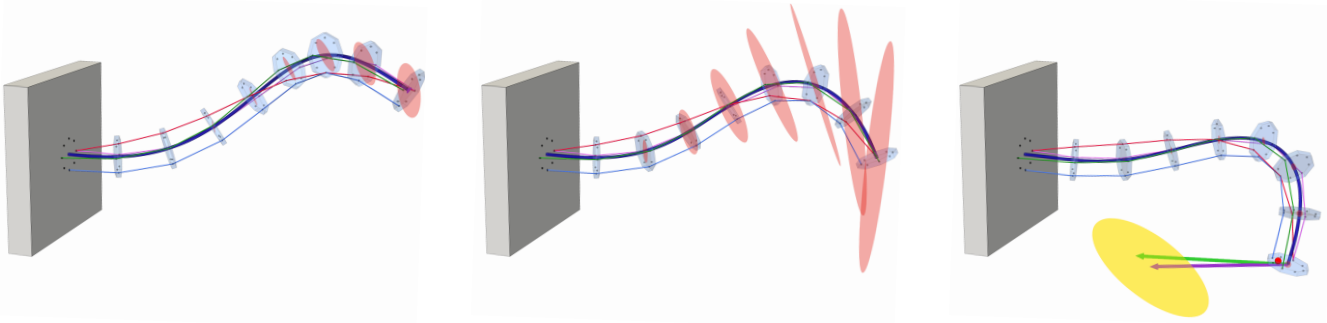


**Fig. 3:** Example snapshots from our tendon robot simulations. *Left*: Forward kinematics with uncertainty. The red ellipses illustrate the position components of pose uncertainty ( $2 - \sigma$ ) along the backbone, subsampled at the disc locations. *Middle*: Prior distribution, given an unknown (zero mean with high prior uncertainty) tip force. *Right*: Posterior tip force distribution, given a noisy tip position measurement (red point). The violet and green arrows indicate the MAP estimate and ground truth forces with force uncertainty (gold). Additionally, the robot tracks the red point throughout our simulation, in spite of the uncertain tip force.

## VI. TENDON ROBOT SIMULATIONS

We evaluate the accuracy, speed, and versatility of our framework on three illustrative tendon robot examples, implemented in simulation (see Fig. 3). Code for running our experiments is at <https://bit.ly/4mj9Bz0> and will later be open-sourced upon publication.

### A. Uncertainty-Aware Kinematics

First, we test our framework in open loop, without any measurement factors, assuming a single tip force. In this application, our solutions can be seen as a forward kinematics model given the inputs  $\mathbf{Q}$  and  $\mathbf{F}_K$  with uncertainty on all variables. In this case, the model considers uncertainty arising from the inputs  $\mathbf{Q}$  and  $\mathbf{F}_K$ , as well as random walk, uncertain boundary conditions, and disc wrench uncertainty (e.g. caused by friction).

We use the resolved-rates Jacobian (18) to generate an open-loop trajectory moving the tip position over set of waypoints. We simulate a time-varying 3D force component of  $\mathbf{F}_K$  whose magnitude pulses smoothly and the direction changes continuously over the unit sphere. Given the inputs, we solved for the MAP estimate at each time step.

To determine numerical accuracy, we compare with a benchmark based on highly accurate numerical integration, using the discrete tendon interaction model [35]. For the benchmark, we directly integrate the Cosserat equations over each segment between two discs, and wrap the ODE in a solver to enforce the boundary conditions as well as the correct tendon/disc interaction loads. We simulated the trajectory using this benchmark and compared the output with our method (both Euler and midpoint rules) while varying the number of discretization nodes. The RMS tip position error results are shown in Fig. 5.

Overall, we can achieve very good ( $< 1\%$ ) position accuracy with relatively few nodes ( $\approx 40$  pose variables), when using the midpoint rule (7) in less than 30 ms. The Euler rule (6) requires did not achieve similar accuracy/speed in our simulations.

### B. Tip Force Sensing

To estimate tip forces, we used simulated tip position measurements, where the measurement model acts as a simple prior factor on the tip pose:

$$\mathbf{z}_p = \text{position}(\mathbf{T}_K) + \mathbf{n}_p, \quad \mathbf{n}_p \sim \mathcal{N}(\mathbf{0}, \Sigma_p); \quad (19)$$

Additionally, since we do not expect tip force or tendon tensions to vary too quickly over time, we also place prior factors from the previous time step on these quantities, based on a heuristic drift covariance:

$$\begin{aligned} \mathbf{F}_K &\sim \mathcal{N}(\mathbf{F}_{\text{prev}}, \Sigma_F^{\text{prev}} + \Sigma_F^{\text{drift}}), \\ \mathbf{Q} &\sim \mathcal{N}(\mathbf{Q}_{\text{prev}}, \Sigma_Q^{\text{prev}} + \Sigma_Q^{\text{drift}}). \end{aligned} \quad (20)$$

This creates a simple temporal motion model ensuring these variables vary smoothly. The overall batch estimation is identical to the forward kinematics, but with these additional factors, and with a large prior on the tip force.

For our simulations, we generate a desired tip position trajectory using waypoints, and use the same  $\mathbf{F}_K$  as in Section VI-A. We simulate ground truth and measurements with the forward kinematics model in Section VI-A, adding Gaussian noise to both tip position and tendon tensions. Given the measurement factors, we estimate the full state—including tip force—online. We use a damped resolved rates control law using (18) to update the commanded tendon tensions for closed loop position tracking, given the estimated force. We also simulate the nominal robot trajectory with no tip force knowledge or compensation, for comparison. An example snapshot is shown in Fig. 3 and results detailed in Fig. 4.

Compared to the uncompensated model, our approach was able to track position over the trajectory, and the force sensing results show reasonable estimates of tip force over time. Additionally, toward the end of the trajectory, the robot encountered an unstable force/shape configuration (jagged lines). In future work with real experiments, we can use the local Jacobian (18), or second order methods to detect and avoid unstable pose/force configurations online.

### C. Distributed Load Estimation

In addition to tip loading, our framework also supports estimating forces distributed along continuum robot backbones

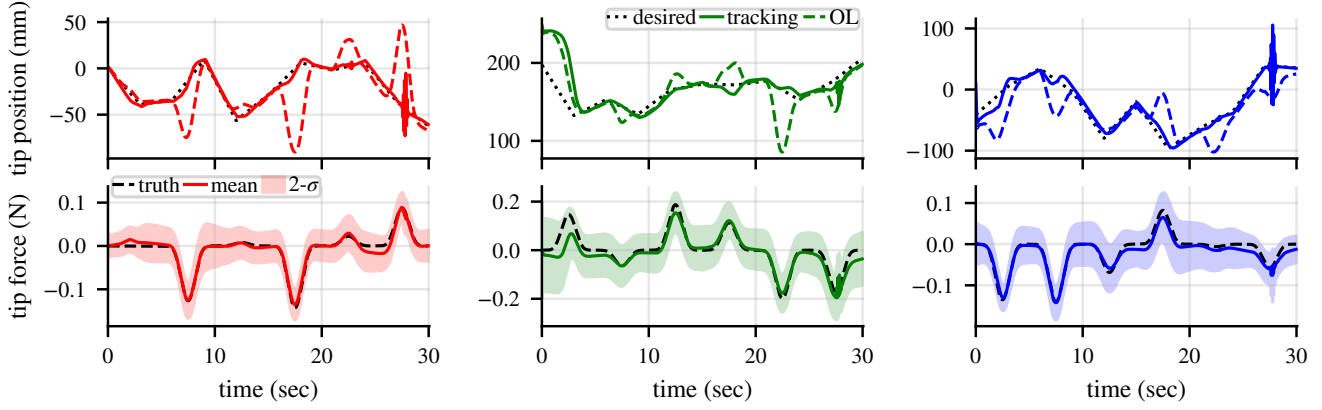


**Fig. 4:** Simulation results showing good trajectory tracking while also estimating unknown tip forces in real time (**26 ms** mean solve time for 900 simulation steps), given noisy tip position feedback. The shaded regions show  $2\sigma$  uncertainty envelopes, and the dotted lines indicate ground truth. For comparison, we additionally show an open-loop (OL) trajectory, with no position feedback.

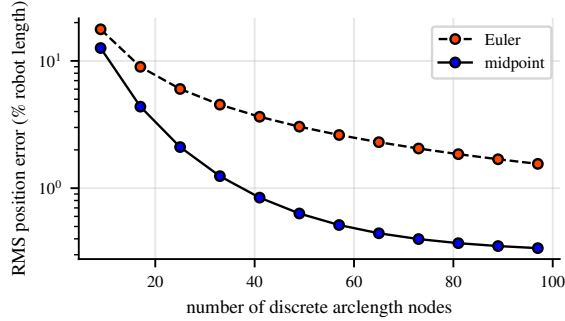


**Fig. 5:** Numerical tip position accuracy of forward kinematics with our approach, compared to a numerical integration benchmark, evaluated over a simulated trajectory. As the number of discretization nodes increases, the MAP tip position approaches the benchmark, and using a midpoint method substantially improves performance.

[5], [20]. To provide a rich set of data for distributed load estimation, we simulate a triaxial FBG array, where each fiber is embedded at the surface of the backbone, spaced evenly at  $120^\circ$ . For each fiber, the axial strain at a point  $\mathbf{r} = (r_x, r_y, 0)$  computed with

$$\mathbf{z}_\epsilon = [0 \ 0 \ 1]^T (\Delta \mathbf{v} - \mathbf{r} \times \Delta \mathbf{u}), \quad \begin{bmatrix} \Delta \mathbf{u} \\ \Delta \mathbf{v} \end{bmatrix} = \mathcal{K}^{-1} \mathbf{S}_k. \quad (21)$$

Stacking the strain measurements for all fibers, the measurement model at a single discretization node is

$$\mathbf{z}_\epsilon = [z_{\epsilon_0} \ z_{\epsilon_1} \ z_{\epsilon_2}]^T + \mathbf{n}_{\epsilon_k}, \quad \mathbf{n}_{\epsilon_k} \sim \mathcal{N}(0, \Sigma_\epsilon). \quad (22)$$

For the entire FBG array, all of such measurements act as prior factors on the internal stress variables  $\mathbf{S}_k$ .

We place an overall zero-mean magnitude prior on each  $\mathbf{F}_k$  with small moment components. Note that we do not require the axial  $z$  components to be zero [5], [20]. To ensure temporal smoothness, we again place priors from the previous time step (20) on each  $\mathbf{F}_k$  and the tensions  $\mathbf{Q}$ . To enforce spatial smoothness, we place a discrete-arclength jerk prior on nearby forces:

$$\mathbf{F}_{k+3} - 3\mathbf{F}_{k+2} + 3\mathbf{F}_{k+1} - \mathbf{F}_k \sim \mathcal{N}(0, \Sigma_F). \quad (23)$$

Together, these *space-time* factors ensure that the estimated force is smooth both along the backbone and over time.

To simulate distributed loads, we first generate a temporal trajectory that purposefully passes through cylindrical obstacles (see Fig. 6). We set the force at each  $k$  to exponentially decay with radial distance from the cylinder, in the direction of the axis. At each time step, noisy FBG outputs are sampled along the robot using the measurement model. Additionally, given the posterior Gaussian for each force, we can detect external loads along the backbone by computing the probability that the force is greater than some threshold  $\tau$ . Figure 6 shows an example result.

## VII. CONCENTRIC TUBE ROBOT APPLICATION

To show the generality of our approach, we additionally apply it to a real-world surgical concentric tube robot. The arm of the Virtuoso system (Figure 7) is comprised of two telescoping tubes, actuated by independently rotating and translating them. Since the outer tube is pre-curved, each arm can reach 3D points in its cone-shaped workspace.

Importantly, since the inner tube is not pre-curved, the tubes do not torsionally interact. Therefore, we model a single arm relatively simply as two Cosserat rods in series. The outer tube is given a prior pose (11) based on its rotation, and its insertion actuation is enforced by choosing an appropriate  $\Delta s$ . The inner tube prior is set similarly by connecting its base pose to the outer tube tip pose. After building the factor graph, we solve the forward kinematics problem and the inverse force sensing problem in a similar way to our tendon robot simulations.

### A. Experiments

We focus on a single arm (left) of the Virtuoso robot, using ROS2 to synchronize and record all data streams from the the tracker, force sensor, and the robot. We collected an initial data set without the robot in order to calibrate the force sensor rotation relative to the tracker. Next, we collected a calibration data set to calibrate the overall setup. For this, the robot was teleoperated to move around its workspace while palpating many points all over the blue

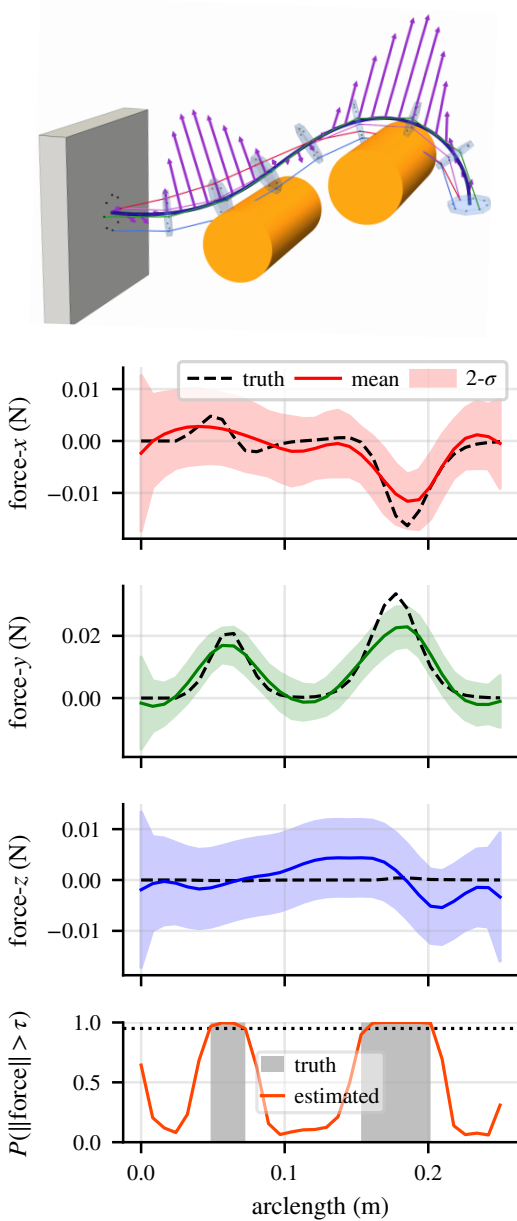


**Fig. 6:** Distributed load estimation at a single point in time in simulation. *Top*: Environmental interaction forces (violet) are estimated along the robot in real time, given noisy FBG strain measurements (**41 ms** mean solve time for 300 simulation steps). *Bottom*: Ground truth comparison. Additionally, we can detect contact along the robot by computing  $p(||\text{force}|| > \tau)$  (orange).

silicone object to impart significant contact forces. Using this data, we performed a joint maximum likelihood optimization to estimate: tracker pose, tracking coil pose, tube curvature, inner/outer tube bending/torsion stiffness, and all actuation noise parameters. We collected a second data set for model evaluation, computing forward kinematics given the measured tip force and tube actuation. An example can be seen in Fig. 8, and detailed results in Fig. 9.

The inverse force sensing problem is solved by using the measured tip position as a prior factor (see Sec. VI-B). Figure 8 shows an example snapshot; we compare the

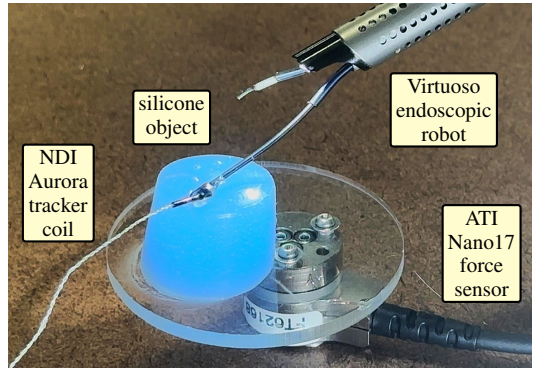


**Fig. 7:** Surgical concentric tube robot experiment setup. The robot was teleoperated to touch a silicone object several times, simulating soft tissue palpation. The object was attached to a force/torque sensor, and a magnetic tracking coil was attached to the tip of the robot to measure tip pose.



**Fig. 8:** Typical forward kinematics and inverse force sensing results from our experiments. Our calibrated forward model (left) can estimate robot state given actuation and tip force (violet). More importantly, given tip position measurements (red dot), the inverse model (right) can estimate unknown tip forces. The red and yellow ellipses indicate position and force uncertainty ( $2\sigma$ ) respectively.

estimated forces to the measured values in Fig. 10.

All of the measured values typically lie within the uncertainty envelopes, indicating good calibration. Given known tip force, our forward kinematics algorithm was able to accurately (**2.35 mm** RMS position error) and efficiently ( **$2.67 \pm 0.39$  ms** solve time) estimate tip position. The inverse force sensing application was also efficient ( **$2.75 \pm 0.37$  ms**) and reasonably accurate (**0.68 N** RMS force error). However, similarly to the tendon robot examples and prior work on force sensing, tip force sensing is ill-conditioned in the axial  $z$  direction, and additional information should be used for fully accurate 3D force sensing.

## VIII. CONCLUSION

We presented a general method for state estimation for continuum robots on  $\text{SE}(3)$ . We first derived a probabilistic Cosserat rod model, and then demonstrated applicability of our method to several sensing problems for tendon-driven robots in simulations, showing real time performance for forward kinematics with uncertainty, tip force sensing, and distributed load estimation. In our experiments, we also applied our approach to a surgical concentric tube robot showing good results for tip force sensing, nodding to future applications in tissue-palpation or haptic feedback.

## REFERENCES

[1] J. Burgner-Kahrs, D. C. Rucker, and H. Choset, “Continuum robots for medical applications: A survey,” *IEEE Transactions on Robotics*, vol. 31, no. 6, pp. 1261–1280, 2015.

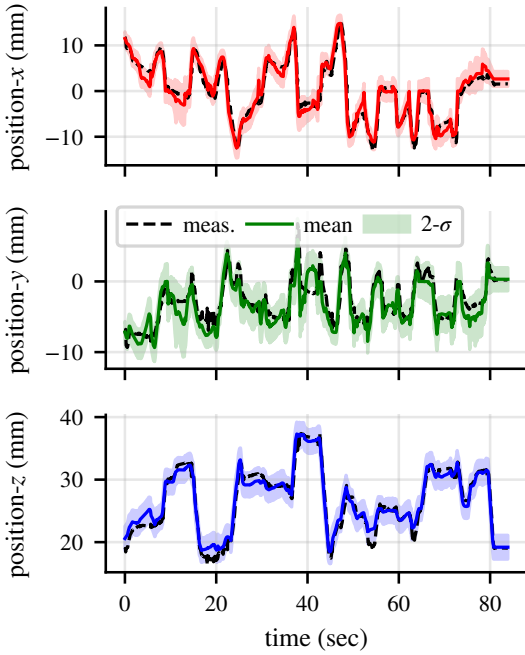


**Fig. 9:** Experimental results for forward kinematic concentric tube robot model. We compare the predicted position mean and uncertainty to the value reported by a magnetic tracker.

- [2] M. Russo, S. M. H. Sadati, X. Dong, A. Mohammad, I. D. Walker, C. Bergeles, K. Xu, and D. A. Axinte, “Continuum robots: An overview,” *Advanced Intelligent Systems*, vol. 5, no. 5, 2023.
- [3] A. W. Mahoney, T. L. Bruns, P. J. Swaney, and R. J. Webster, “On the inseparable nature of sensor selection, sensor placement, and state estimation for continuum robots,” in *IEEE International Conference on Robotics and Automation*, 2016, pp. 4472–4478.
- [4] P. L. Anderson, A. W. Mahoney, and R. J. Webster, “Continuum reconfigurable parallel robots for surgery: Shape sensing and state estimation with uncertainty,” *IEEE robotics and automation letters*, vol. 2, no. 3, pp. 1617–1624, 2017.
- [5] J. M. Ferguson, D. C. Rucker, and R. J. Webster, “Unified shape and external load state estimation for continuum robots,” *IEEE Transactions on Robotics*, vol. 40, pp. 1813–1827, 2024.
- [6] T. D. Barfoot, *State estimation for robotics*. Cambridge University Press, 2017.
- [7] C. Forster, L. Carlone, F. Dellaert, and D. Scaramuzza, “On-manifold preintegration for real-time visual-inertial odometry,” *IEEE Transactions on Robotics*, vol. 33, no. 1, pp. 1–21, 2016.
- [8] M. Kaess, H. Johannsson, R. Roberts, V. Ila, J. J. Leonard, and F. Dellaert, “isam2: Incremental smoothing and mapping using the bayes tree,” *The International Journal of Robotics Research*, vol. 31, no. 2, pp. 216–235, 2012.
- [9] F. Dellaert, “Factor graphs: Exploiting structure in robotics,” *Annual Review of Control, Robotics, and Autonomous Systems*, vol. 4, no. 1, pp. 141–166, 2021.
- [10] S. Lilge, T. D. Barfoot, and J. Burgner-Kahrs, “Continuum robot state estimation using gaussian process regression on  $se(3)$ ,” *The International Journal of Robotics Research*, vol. 41, no. 13–14, pp. 1099–1120, 2022.
- [11] ———, “State estimation for continuum multi-robot systems on  $se(3)$ ,” *IEEE Transactions on Robotics*, 2024.
- [12] F. Dellaert, “Factor graphs and gtsam: A hands-on introduction,” *Georgia Institute of Technology, Tech. Rep.*, vol. 2, no. 4, 2012.
- [13] D. B. Camarillo, K. E. Loewke, C. R. Carlson, and J. K. Salisbury, “Vision based 3-d shape sensing of flexible manipulators,” in *IEEE International Conference on Robotics and Automation*, 2008, pp. 2940–2947.
- [14] M. W. Hannan and I. D. Walker, “Real-time shape estimation for continuum robots using vision,” *Robotica*, vol. 23, no. 5, pp. 645–651, 2005.

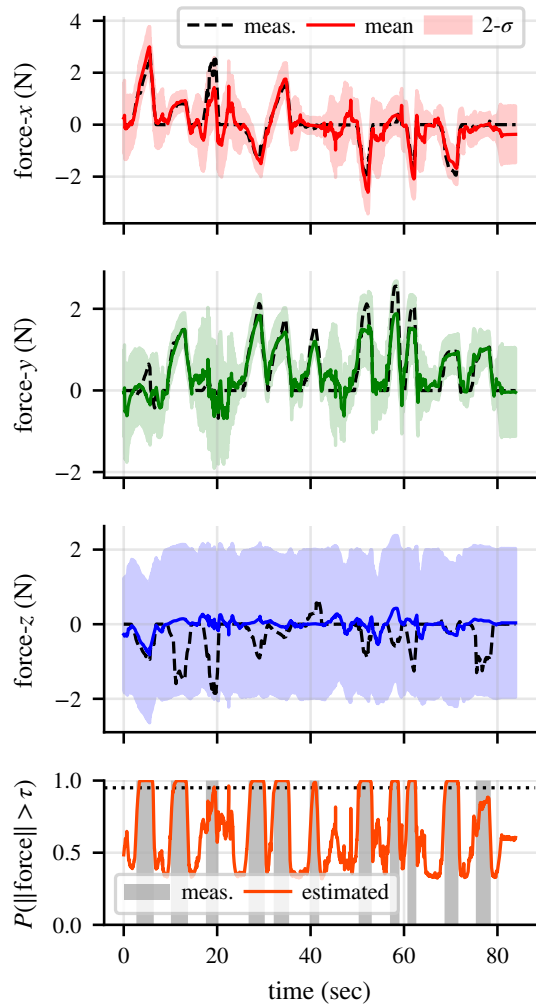


**Fig. 10:** Experimental results for concentric tube robot force sensing. We compare the predicted 3D force mean and uncertainty to the value reported by a force sensor (top three plots). Note that since the robot is stiff in the axial direction, inference typically returns the prior for the  $z$  direction. We can detect contact by computing the probability that the force exceeds a threshold (bottom).

- [15] B. Kim, J. Ha, F. C. Park, and P. E. Dupont, “Optimizing curvature sensor placement for fast, accurate shape sensing of continuum robots,” in *IEEE international conference on robotics and automation*, 2014, pp. 5374–5379.
- [16] V. Modes, T. Ortmaier, and J. Burgner-Kahrs, “Shape sensing based on longitudinal strain measurements considering elongation, bending, and twisting,” *IEEE Sensors Journal*, vol. 21, no. 5, pp. 6712–6723, 2020.
- [17] S. C. Ryu and P. E. Dupont, “Fbg-based shape sensing tubes for continuum robots,” in *IEEE International Conference on Robotics and Automation*, 2014, pp. 3531–3537.
- [18] Q. Zhao, J. Lai, K. Huang, X. Hu, and H. K. Chu, “Shape estimation and control of a soft continuum robot under external payloads,” *IEEE/ASME Transactions on Mechatronics*, vol. 27, no. 5, pp. 2511–2522, 2021.
- [19] C. B. Black, J. Till, and D. C. Rucker, “Parallel continuum robots: Modeling, analysis, and actuation-based force sensing,” *IEEE Transactions on Robotics*, vol. 34, no. 1, pp. 29–47, 2017.
- [20] V. Aloi, K. T. Dang, E. J. Barth, and C. Rucker, “Estimating forces along continuum robots,” *IEEE Robotics and Automation Letters*, vol. 7, no. 4, pp. 8877–8884, 2022.
- [21] D. C. Rucker and R. J. Webster, “Deflection-based force sensing for continuum robots: A probabilistic approach,” in *IEEE/RSJ International Conference on Intelligent Robots and Systems*, 2022, pp. 1–8.

*tional Conference on Intelligent Robots and Systems*, 2011, pp. 3764–3769.

[22] A. Brij Koolwal, F. Barbagli, C. Carlson, and D. Liang, “An ultrasound-based localization algorithm for catheter ablation guidance in the left atrium,” *The International Journal of Robotics Research*, vol. 29, no. 6, pp. 643–665, 2010.

[23] J. A. Borgstadt, M. R. Zinn, and N. J. Ferrier, “Multi-modal localization algorithm for catheter interventions,” in *IEEE international conference on robotics and automation*, 2015, pp. 5350–5357.

[24] Q. Qiao, G. Borghesan, J. De Schutter, and E. Vander Poorten, “Force from shape—estimating the location and magnitude of the external force on flexible instruments,” *IEEE Transactions on Robotics*, vol. 37, no. 5, pp. 1826–1833, 2021.

[25] O. Weeger, S.-K. Yeung, and M. L. Dunn, “Isogeometric collocation methods for cosserat rods and rod structures,” *Computer Methods in Applied Mechanics and Engineering*, vol. 316, pp. 100–122, 2017.

[26] A. L. Orekhov and N. Simaan, “Solving cosserat rod models via collocation and the magnus expansion,” in *IEEE/RSJ International Conference on Intelligent Robots and Systems*, 2020, pp. 8653–8660.

[27] S. H. Sadati, S. E. Naghibi, I. D. Walker, K. Althoefer, and T. Nanayakkara, “Control space reduction and real-time accurate modeling of continuum manipulators using ritz and ritz–galerkin methods,” *IEEE Robotics and Automation Letters*, vol. 3, no. 1, pp. 328–335, 2017.

[28] S. Grazioso, G. Di Gironimo, and B. Siciliano, “A geometrically exact model for soft continuum robots: The finite element deformation space formulation,” *Soft robotics*, vol. 6, no. 6, pp. 790–811, 2019.

[29] M. Xie and F. Dellaert, “A unified method for solving inverse, forward, and hybrid manipulator dynamics using factor graphs,” *arXiv preprint arXiv:1911.10065*, 2019.

[30] M. Xie, A. Escontrela, and F. Dellaert, “A factor-graph approach for optimization problems with dynamics constraints,” *arXiv preprint arXiv:2011.06194*, 2020.

[31] J.-L. Blanco-Claraco, A. Lanza, and G. Reina, “A general framework for modeling and dynamic simulation of multibody systems using factor graphs,” *Nonlinear Dynamics*, vol. 105, no. 3, pp. 2031–2053, 2021.

[32] J. Dong, M. Mukadam, F. Dellaert, and B. Boots, “Motion planning as probabilistic inference using gaussian processes and factor graphs,” in *Robotics: Science and Systems*, vol. 12, no. 4, 2016, pp. 10–15 607.

[33] D. K. Pai, “Strands: Interactive simulation of thin solids using cosserat models,” in *Computer graphics forum*, vol. 21, no. 3, 2002, pp. 347–352.

[34] F. Renda, F. Boyer, J. Dias, and L. Seneviratne, “Discrete cosserat approach for multisection soft manipulator dynamics,” *IEEE Transactions on Robotics*, vol. 34, no. 6, pp. 1518–1533, 2018.

[35] A. Gao, Y. Zou, Z. Wang, and H. Liu, “A general friction model of discrete interactions for tendon actuated dexterous manipulators,” *Journal of Mechanisms and Robotics*, vol. 9, no. 4, p. 041019, 2017.